Study of perpendicular anisotropy $L1_0$-FePt pseudo spin valves using a micromagnetic trilayer model

Pin Ho,[1,2,a)] Richard F. L. Evans,[3] Roy W. Chantrell,[3] Guchang Han,[2] Gan-Moog Chow,[1] and Jingsheng Chen[1]
[1]*Department of Materials Science and Engineering, National University of Singapore, 117576 Singapore*
[2]*Data Storage Institute, Agency of Science, Technology and Research (A*STAR), 117608 Singapore*
[3]*Department of Physics, University of York, York YO10 5DD, United Kingdom*

(Received 5 March 2015; accepted 18 May 2015; published online 1 June 2015)

A trilayer micromagnetic model based on the Landau-Lifshitz-Bloch equation of motion is utilized to study the properties of $L1_0$-FePt/TiN/$L1_0$-FePt pseudo spin valves (PSVs) in direct comparison with experiment. Theoretical studies give an insight on the crystallographic texture, magnetic properties, reversal behavior, interlayer coupling effects, and magneto-transport properties of the PSVs, in particular, with varying thickness of the top $L1_0$-FePt and TiN spacer. We show that morphological changes in the FePt layers, induced by varying the FePt layer thickness, lead to different hysteresis behaviors of the samples, caused by changes in the interlayer and intralayer exchange couplings. Such effects are important for the optimization of the PSVs due to the relationship between the magnetic properties, domain structures, and the magnetoresistance of the device. [http://dx.doi.org/10.1063/1.4921828]

I. INTRODUCTION

In recent years, there has been a surge in interest in the applications of giant magnetoresistance (GMR) spin valves and magnetic tunneling junctions (MTJs) with perpendicular magnetic anisotropy (PMA) in areas of spintronics, such as spin transfer torque magnetic random access memory (STT-MRAM) and spin torque oscillators.[1–5] This is driven by the promise of extremely high areal density and thermal stability offered by spin valves and MTJs with PMA.[6–8] $L1_0$-FePt is a favored candidate in spin valves and MTJs due to its high magnetocrystalline anisotropy (K_u) of 7×10^7 erg/cc leading to a high degree of thermal stability.[9] As such, recent efforts have been made on the study of $L1_0$-FePt as the ferromagnetic (FM) layer in spin valves and MTJs.[10–15] $L1_0$-FePt based pseudo spin valves (PSV) with the use of an Ag spacer have been reported to yield a high GMR of 1.1% compared to spacers, such as Pd and Pt.[10,11] Yoshikawa *et al.* demonstrated that $L1_0$-FePt MTJs with MgO spacer produced a tunneling magnetoresistance (MR) of 110% using current-in-plane (CIP) tunneling measurements.[12] The application of the $L1_0$-FePt/Au/$L1_0$-FePt spin valve structure for STT-MRAM has also been achieved by Seki *et al.*[13]

More recently, $L1_0$-FePt based PSVs with TiN spacer have been reported.[14,15] TiN is deemed a suitable material for the spacer due to its excellent diffusion barrier properties and the desirable quality of being chemically stable with respect to FePt. The strain from the large lattice mismatch of 9.5% between FePt and TiN also induces an additional perpendicular interface anisotropy in the $L1_0$-FePt. Metallic TiN has low resistivity of 15×10^{-6} ohm cm (Ref. 14) and electron mean free path in the range of 39–41 nm.[15] The large electron mean free path of TiN allows electrons to pass through the TiN spacer and across the TiN spacer/$L1_0$-FePt ferromagnets interfaces with a small probability of undergoing spin independent scattering. First principles calculations show that near the Fermi energy level of 0 eV, the energy band structures of the FePt spin up electrons displayed better band structure matching with TiN, in terms of more similar energy and slope, compared to that of FePt spin down electrons with TiN.[14] This implied a higher transmission of the majority spin up electrons across the $L1_0$-FePt/TiN interface, and resistivity changes due to the spin dependent scattering of the conduction electrons at the trilayer interfaces are expected.

In addition to the layer-wise structure, the in-plane structural properties are of particular importance to the overall magnetic and magnetoresistive properties of the device. A schematic showing the operation of a PSV is shown in Fig. 1. A spin valve principally consists of two magnetic

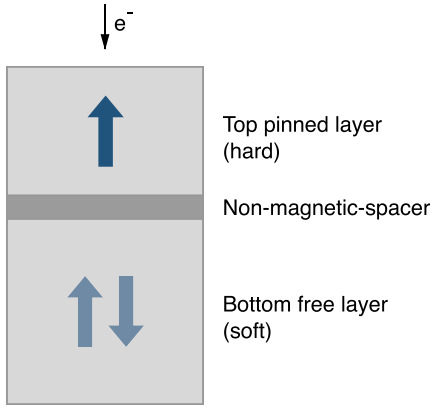

FIG. 1. Schematic illustration of the operation of the PSV. The orientation of the top layer is fixed and polarizes the incoming electrons. The orientation of the soft bottom layer is controlled by an external applied field. The resistance of the device depends on the orientation of the two FM layers which gives rise to the magnetoresistance.

a)hopin@mit.edu

layers, one magnetically hard and the other magnetically soft, so that one is effectively pinned, and the other is free. Depending on the application, the anisotropy of the soft layer is different: for sensors, the free layer has the lowest possible anisotropy, while for MRAM applications, the soft layer should be thermally stable for some time. Current GMR spin valve sensors utilize a granular IrMn structure[16] to enable tight control of the pinned layer properties by exchange biasing. In a PSV, the hard magnetic layer provides the reference magnetic layer and so must have a high anisotropy, while the soft layer must switch at lower applied fields. In thin films and patterned nanostructures, magnetostatic effects often display a dominant effect on the hysteresis properties. Thus, to ensure a controllable and high coercivity, the materials are made granular with each grain consisting of a single domain. Although each grain is essentially a single domain particle, the grains are subjected to magnetostatic interactions which lead to a complicated macroscopic hysteresis behavior. In addition, due to the long range order of the exchange interaction, the physical separation of grains does not always guarantee complete exchange decoupling. In general, the effects of interactions are complex, but understanding them is crucial to the tailoring of the magnetic properties (and by extension of the magnetoresistive properties) of a PSV device.

Significant research efforts have been made on the study of spin valves and MTJs but theoretical studies remain limited thus far. Earlier accounts include the atomistic[17] and bilayer micromagnetic[18] modeling of $L1_0$-FePt based PSVs, dealing mainly with the effects of interlayer diffusion within the $L1_0$-FePt/Ag/$L1_0$-FePt PSVs. The atomistic study involved a single grain model which did not take into consideration either inter-grain exchange coupling or magnetostatic interactions present in realistic granular $L1_0$-FePt films. While a more complete model of the spin valve was made with the bilayer micromagnetic model,[18] the model was a dual layer ferromagnetic system which did not explicitly include the presence of a non-magnetic spacer.

In this paper, we measure experimentally and model theoretically the magnetic and magnetoresistive properties of a trilayer $L1_0$-FePt/TiN/$L1_0$-FePt PSV. In particular, we investigate the effects of the thickness of the top $L1_0$-FePt and TiN spacer layers on the crystallographic texture, magnetic properties, reversal behavior, interlayer coupling effects, and magneto-transport properties of the device.

II. EXPERIMENTAL DETAILS

In the experimental work, the top $L1_0$-FePt thickness in the PSV, with the structure MgO (001) substrate/$L1_0$-FePt (20 nm)/TiN (5 nm)/$L1_0$-FePt (x nm), was varied with $x = 5$, 10, 15, and 20 nm. The TiN spacer thickness in MgO (001) substrate/$L1_0$-FePt (20 nm)/TiN (y nm)/$L1_0$-FePt (20 nm) was varied with $y = 3$, 4, 5, 6, and 7 nm. The samples were prepared using a magnetron sputtering system with a base pressure better than 8×10^{-7} Torr. In all of these samples, the TiN spacer was deposited at 350 °C. The bottom and top $L1_0$-FePt layers were deposited at 400 and 500 °C, respectively, giving rise to different degrees of $L1_0$ ordering. Thus, the bottom $L1_0$-FePt possessed a smaller coercivity and behaved as the free layer. Magnetic properties were characterized using a vibrating sample magnetometer (VSM). Surface roughness and magnetic domain configurations were probed using atomic force microscopy (AFM) and magnetic force microscopy (MFM), respectively. CIP resistance measurements were made using a four point probe in the presence of a perpendicular-to-plane field. The film nanostructure was determined using scanning electron microscopy (SEM).

III. MICROMAGNETIC MODEL

The FePt/TiN/FePt trilayer is modeled by considering two FePt magnetic layers separated by a non-magnetic spacer. Each FePt layer is made up of grains with a mean grain size of 20 nm as shown schematically in Fig. 2. It is necessary to partition the FePt layers into grains for the implementation of varying degrees of interlayer and intralayer interactions, which will be elaborated later. The grain structure in the plane is modeled using a two-dimensional Voronoi construction, represented by hexagonal shaped grains that form a honeycomb Voronoi tessellation, which naturally leads to a grain size distribution as well as a distribution in the exchange coupling between neighboring grains due to the dispersion in contact area. Each grain is small enough to be considered a single domain, and is modeled using the micromagnetic Landau-Lifshitz-Bloch (LLB) equation of motion.[19] The primary advantage of the LLB approach over the more commonly used Landau-Lifshitz-Gilbert equation is the natural treatment of thermal effects, including the distinct transverse and longitudinal magnetization fluctuations as well as the ability to simulate heating through the Curie point. Although high temperatures are not relevant for this work (all simulations are performed at room temperature), the LLB generally provides a more rigorous micromagnetic formalism valid at all temperatures and as such is a better approach. The parameters used for the $L1_0$-FePt magnetic layers are derived from density functional theory and atomistic spin simulations using a multi-scale approach described in detail in Ref. 20. The only alteration made to the parameters is the scaling of the anisotropy (given by the transverse susceptibility) to represent different degrees of chemical $L1_0$ ordering in the two layers. In order to represent the thermodynamic thermal fluctuations, we use

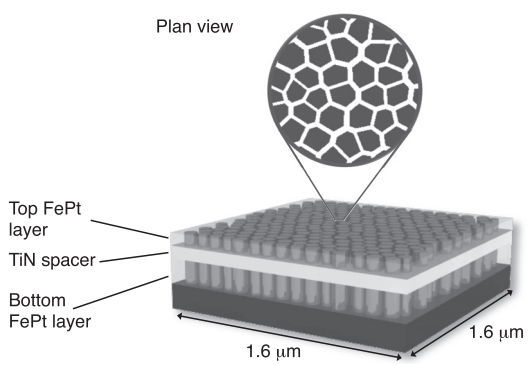

FIG. 2. Schematic illustration of the trilayer model adopted in the micromagnetic simulation showing the multilayer structure.

the stochastic form of the LLB where the equation of motion for each grain is given by[21]

$$\dot{\mathbf{m}} = \gamma[\mathbf{m} \times \mathbf{H}_{\text{eff}}] + \frac{|\gamma|\alpha_{||}}{m^2}(\mathbf{m} \cdot \mathbf{H}_{\text{eff}})\mathbf{m} - \frac{|\gamma|\alpha_{\perp}}{m^2}[\mathbf{m} \times [\mathbf{m} \times (\mathbf{H}_{\text{eff}} + \boldsymbol{\eta}_{\perp})]] + \boldsymbol{\eta}_{||}, \quad (1)$$

where $m = M_s/M_0$ is the magnetization normalized to its zero-temperature value, γ is the gyromagnetic ratio, $\alpha_{||}$ and $\alpha_{\perp}$ are the dimensionless temperature dependent longitudinal and transverse damping parameters, and $\boldsymbol{\eta}_{\perp}$ and $\boldsymbol{\eta}_{||}$ are the transverse and longitudinal noise terms, respectively, given by

$$\begin{aligned} \langle \eta_i^{\mu} \rangle &= 0, \\ \langle \eta_i^{\perp}(0)\eta_j^{\perp}(t) \rangle &= \frac{2k_B T(\alpha_{\perp} - \alpha_{||})}{|\gamma| M_s^0 V \alpha_{\perp}^2}\delta_{ij}\delta(t), \\ \langle \eta_i^{||}(0)\eta_j^{||}(t) \rangle &= \frac{2|\gamma|k_B T\alpha_{||}}{M_s^0 V}\delta_{ij}\delta(t), \\ \langle \eta_i^{||}\eta_j^{\perp} \rangle &= 0. \end{aligned} \quad (2)$$

The effective field $\mathbf{H}_{\text{eff}}$ below T_c is given by

$$\mathbf{H}_{\text{eff}} = \mathbf{H} - \frac{\left(m_x^2 + m_y^2\right)}{\tilde{\chi}_{\perp}} + \frac{1}{2\tilde{\chi}_{||}}\left(1 - \frac{m^2}{m_e^2}\right)\mathbf{m}, \quad (3)$$

where $\tilde{\chi}_{||} = (dm/dH)_{H \to 0}$ is the longitudinal susceptibility, $\tilde{\chi}_{\perp}$ is the transverse susceptibility, and m_e is the equilibrium magnetization.[20]

The grain size is kept at 20 nm, typical of $L1_0$-FePt films.[22] Each simulated FePt layer consists of a total of 6400 grains. With 80 grains on each edge of the simulated sample, a sample dimension of $1.6\,\mu\text{m} \times 1.6\,\mu\text{m}$ is simulated. Epitaxial behavior across the FePt/TiN/FePt trilayer is modeled with an array of perpendicularly magnetized top FePt grains grown grain-on-grain on the bottom FePt grains. The spacer is introduced with the insertion of a physical space between the two FePt layers, where the spacer thickness is represented by the magnitude of the gap between the two FePt layers. An abrupt and sharp FePt/TiN interface is assumed in line with the fact that TiN is an excellent diffusion barrier and is chemically stable towards FePt. Magnetostatic interactions between the grains were included using the dipole approximation,[23,24] which is reasonable given the near-spherical grain dimensions.

Within the top and bottom FePt layers, the inter-grain interaction is controlled by the strength of the intralayer exchange interaction field (H_{intra}), exchange field dispersion (d_{intra}), and fraction of exchange decoupled grains (f_{intra}). The exchange interaction field $\mathbf{H}_i^e$ acting on a grain i within each FePt layer is approximated using the following equation:[25]

$$\mathbf{H}_i^e = H_{exchange}\sum_{i \neq j} f_{ij}\frac{A_i}{A_m}\frac{L_m}{L_i}\hat{\mathbf{m}}_j, \quad (4)$$

where the sum is taken over nearest neighbors. $\hat{\mathbf{m}}_j$ is the unit direction of magnetization in a neighboring grain, $H_{exchange}$ is the mean exchange interaction field, A_i is the contact area, L_i is the contact length, A_m is the mean contact area, and L_m is the mean contact length between the two neighboring FePt grains. These factors are determined entirely by the grain structure created by the Voronoi construction. Disorder in the exchange interaction between the grains is introduced through a normalized probability distribution f_{ij} which has two components. Firstly, it comprises a Gaussian distribution, which represents the dispersion of intrinsic exchange coupling between individual grains. This arises from the dependence of the exchange coupling on the intergranular separation[26,27] and the variation in the properties of individual grain boundaries arising from dispersion in the local chemical composition. Furthermore, we introduce a fraction of grains f_{intra} which are fully exchange decoupled to better represent the microstructure.

Interlayer interactions between the FM layers will directly affect the independent switching of the magnetic layers and hence the performance of the spin valve or MTJ, in particular, its MR. There are several origins of the interlayer coupling:[28–32] magnetostatic effects due to the magnetic dipoles of the individual magnetic grains will be present in the PMA PSVs; direct interlayer exchange coupling occurs in the presence of the pinholes within the spacer layer; indirect oscillatory coupling also arises due to the Ruderman-Kittel-Kasuya-Yosida (RKKY) interactions, which originate from the quantum interference of electrons confined within the non-magnetic spacer. This RKKY contribution is assumed to be negligible in the $L1_0$-FePt/TiN/$L1_0$-FePt PSVs, given the relatively large length scale of the TiN spacer thickness. We now consider the interlayer exchange interaction field acting between two adjacent epitaxial grains across the non-magnetic layer. In this case, the number of atoms in the contact area is $N = A_i/a^2$ and the exchange energy between layers 1 and 2 can be written as

$$E_{int}^{i,12} = -NJ_i^{int}\hat{\mathbf{S}}_{i,1} \cdot \hat{\mathbf{S}}_{i,2}, \quad (5)$$

where $\hat{\mathbf{S}}_{i1,2}$ are the unit vectors of the spins of grain i in layer 1, 2 and J_i^{int} is the interlayer exchange coupling. The field on layer 1 due to layer 2 is

$$\mathbf{H}_e^{i1,2} = -\frac{\partial E_{int}^{i1,2}}{\partial M_s V_{i1}} = \frac{A_i J_i^{int}}{a^2 M_s A_i t_{1,2}}\hat{\mathbf{m}}_{i2}, \quad (6)$$

where $\hat{\mathbf{m}}_{i2} \equiv \hat{\mathbf{S}}_{i2}$ is the magnetization vector of grain i in layer 2 and $t_{1,2}$ is the physical separation between layers 1 and 2. Similarly one can derive an expression for the field on layer 1 due to layer 2, and finally

$$\mathbf{H}_e^{i1,2} = H_{int}^{i1,2}\hat{\mathbf{m}}_{i2,1}, \quad (7)$$

where

$$H_{int1,2} = \frac{J_i^{int}}{a^2 M_s t_{1,2}}. \quad (8)$$

As in the case for the intra-layer exchange, we introduce disorder in the exchange coupling through a normalized probability distribution, f_{inter}^i, with the same two component standard deviation, leading to

$$\mathbf{H}_{\alpha}^{i} = f_{inter}^{i} H_{int,\alpha,\beta} \hat{\mathbf{m}}_{i\beta}, \quad (9)$$

where α, β label the individual layers, f_{inter}^{i} is a probability distribution analogous to f_{ij}^{i}, and $H_{int,\alpha,\beta}$ is the mean value of the interlayer exchange field.

IV. RESULTS

We carried out an extensive experimental and computational investigation of the properties of the trilayer PSV structures. The aim is to determine the effects of exchange and magnetostatic interactions on the magnetic and transport properties of the structures. In Secs. IV A–IV C, we present a study of their hysteresis behavior, coupled with MFM measurement and simulation of domain structures in both layers. The combination of macro- and micro-scopic investigations allows the determination of the exchange coupling parameters for the structure. Finally, we present the results of GMR measurements and simulations, which are consistent with the macroscopic hysteresis measurements within a simple model.

A. Microstructural and magnetic effects of the top layer thickness

The principle of operation of PSVs is that each of the two layers has a different switching field, where one layer typically has a much higher coercivity than the other. FePt is an excellent candidate material since in its as-deposited form, it adopts a disordered face-centred-cubic ordering which is magnetically soft. With annealing, the FePt undergoes a phase transition to the $L1_0$ form which has a very high magnetic anisotropy. Experimentally, our samples possess different degrees of magnetic ordering due to the different deposition temperatures of the layers. The soft bottom $L1_0$-FePt behaved as the free layer, while hard top $L1_0$-FePt the fixed layer.

We first investigate the effects of the top harder layer thickness on the magnetic properties of the device. Changing the FePt layer thickness leads to changes in morphology which principally affect two key phenomena: specifically, the intergranular exchange coupling and an increased influence of the dipole field between the layers. The changes in morphology of the top layer for different layer thicknesses are shown in the SEM images in Fig. 3. Increasing the top $L1_0$-FePt layer thickness changes the granular nature of the film to a more complete continuous 3D growth, due to agglomeration of the grains. This suggests that a greater proportion of grains in the top layer is exchange coupled at greater film thicknesses. Thus, we expect the fraction of intralayer decoupled grains f_{intra} for the top $L1_0$-FePt to diminish with increasing top $L1_0$-FePt thickness. In addition, we note that according to Eq. (8), we expect a decrease in the interlayer exchange coupling field (H_{int}) with increasing hard layer thickness.

In the simulated trilayers with varying top $L1_0$-FePt thickness, the anisotropy of the top and bottom $L1_0$-FePt is kept constant at 1.31×10^7 erg/cc and 8.48×10^6 erg/cc, respectively, due to the different deposition temperatures of the layers and commensurate degree of $L1_0$ ordering. Both the $L1_0$-FePt layers are assumed to have an intralayer exchange field $H_{\text{intra}} = 35$ kOe. A small dispersion in the exchange field of 0.1 within (d_{intra}) and between (d_{inter}) both $L1_0$-FePt layers is introduced to represent the non-uniformity of exchange coupling due to defects. The fraction of decoupled grains f_{intra} for the bottom $L1_0$-FePt and the fraction of decoupled grains between the $L1_0$-FePt layers f_{inter} are fixed at 0.01 and 0.8, respectively, representing the semi-continuous nature of the film in the bottom layer, and also, the much weaker degree of coupling between the layers due to the addition of the spacer layer. AFM images (not shown here) show a more granular island film for the hard top $L1_0$-FePt layer compared to the bottom $L1_0$-FePt layer with a lower ordering. As such, a larger value is expected of the f_{intra} for the top $L1_0$-FePt layer. The changes in the values of the f_{intra} for the top $L1_0$-FePt and the H_{int} are summarized in Table I. It can be seen that the product of the hard layer thickness and H_{int} is approximately constant, suggesting that the intrinsic interlayer exchange coupling J_i^{int} is insensitive to the hard layer thickness. This implies that the nature of the interlayer is not strongly affected by the hard layer thickness, whose most significant effect is to give rise to more uniform intralayer coupling.

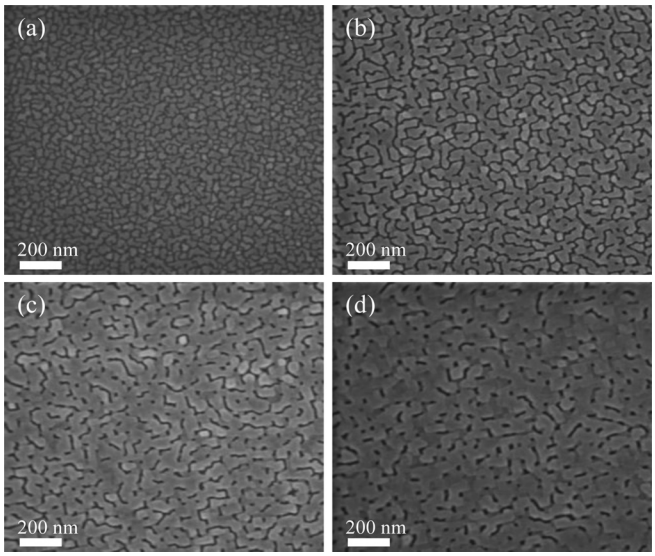

FIG. 3. Plan-view SEM images of top $L1_0$-FePt with thickness of (a) 5,[14] (b) 10, (c) 15, and (d) 20 nm (Ref. 14) for the MgO/$L1_0$-FePt/TiN/$L1_0$-FePt PSVs. The grain structure becomes more continuous with increasing layer thickness leading to lower fraction of exchange decoupled grains.

Having considered the effects of film morphology on the magnetic parameters, we now consider the hysteresis behavior of the various samples in comparison to the modeling results, as shown in Figs. 4 and 5 for the different hard layer thicknesses. The aim of the investigation is to obtain an

TABLE I. A summary of the magnetic properties of the simulated trilayers with varying top FePt thickness of 5–20 nm.

Top FePt thickness (nm)	Top f_{intra}	H_{int} (kOe)
5	0.4	5.00
10	0.3	2.25
15	0.2	1.50
20	0.1	1.20

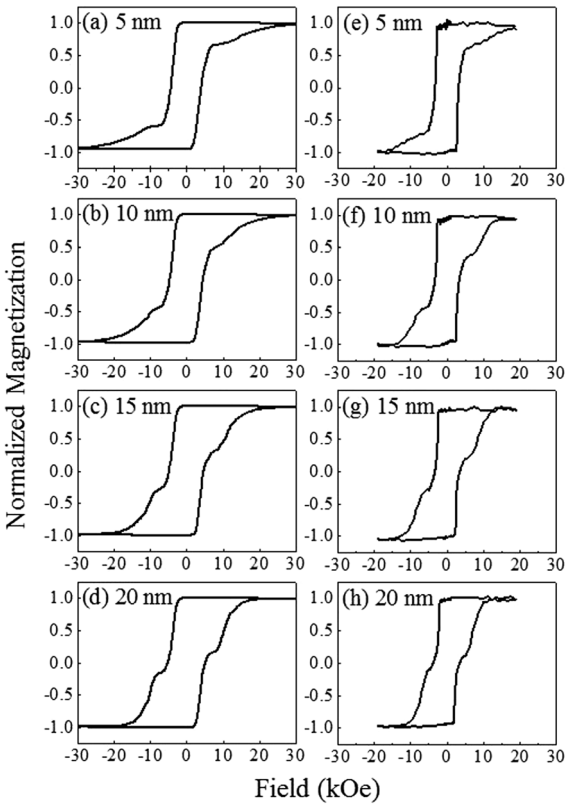

FIG. 4. Out-of-plane hysteresis loops with top FePt thickness of (a) 5, (b) 10, (c) 15, and (d) 20 nm for the simulated trilayer. Out-of-plane hysteresis loops measured at room temperature with top $L1_0$-FePt thickness of (e) 5, (f) 10, (g) 15, and (h) 20 nm for the fabricated MgO/$L1_0$-FePt/TiN/$L1_0$-FePt PSVs.[14]

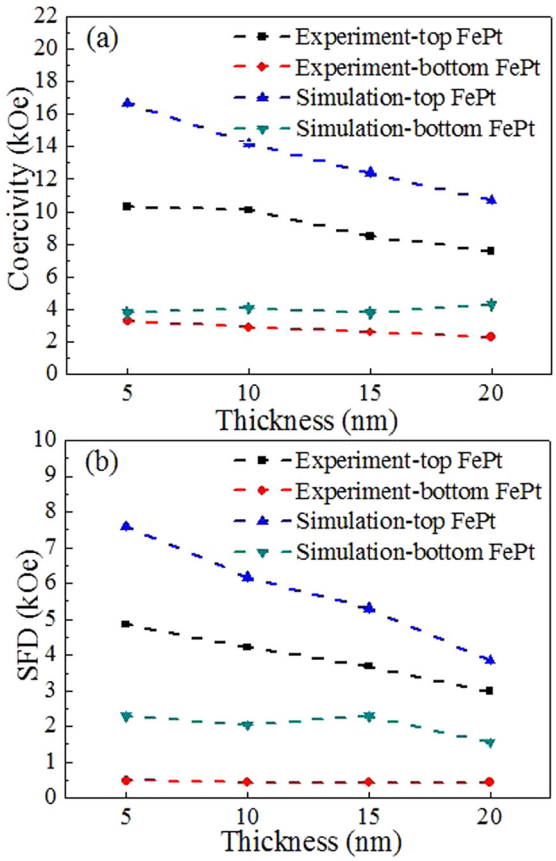

FIG. 5. (a) Coercivity and (b) SFD of the top and bottom FePt layers from simulation and experiment as a function of the top FePt thickness. Dashed lines serve as a guide for the eyes.

understanding of the behavior of the films by fitting the theoretical model to experimental data. Firstly, we describe the fits to the hysteresis loops (Figs. 4 and 5). This process cannot be guaranteed to give an unambiguous determination of the intrinsic material parameters, so we have also ensured that the parameters give simultaneously a good description of the domain structures determined by MFM imaging as will be described later. Qualitatively, the agreement between the model predictions and experiments for the simulated magnetization behavior of the trilayers with varying top $L1_0$-FePt thickness is very good (Fig. 4). The shape of the loop changes consistently for both simulation and experiment as the contribution of the top FePt layer to the total magnetization changes. In both experiment and simulation, the coercivity of the top hard layer decreases with increasing thickness, while the bottom soft layer does not change appreciably with varying top layer thickness [Fig. 5(a)]. However, we note that the coercivity of the simulated trilayers is approximately 1.5 times larger than that of the actual measurement. This deviation is likely contributed by the disparity in the time dependent measurement of the hysteresis loops, which are computed over a few nanoseconds, compared to the experiments where a longer measurement time allowed sufficient time for spin relaxation.[33]

The loops display a characteristic form which varies systematically with the thickness of the top FePt layer (Fig. 4). There are two principal features, each of which can be associated with different layers of the film. The initial feature is a sharp decrease in the magnetization at a nucleation field which is essentially independent of the top FePt layer. Inspection of the loops shows that the size of the initial feature scales with t_b/t, where t_b and t are the thickness of the bottom layer and the total thickness, respectively. This suggests that the initial step is associated with the soft bottom layer. The behavior of the bottom layer is consistent with the nucleation and propagation of a large-scale domain structure. We conclude that the bottom layer comprises strongly coupled grains, reflected in the large intra-layer exchange coupling required to obtain agreement with experiment. This will be considered later in relation to the simulated and experimental magnetization structures.

The second feature of the hysteresis loops is the pronounced "tail" at high fields. The scaling of the steps in the loop suggests that this is associated with the hard top FePt layer. The hysteresis loop associated with the top layer is relatively wide (Fig. 4), indicating a large switching field distribution (SFD). The SFD was determined from the full width half maximum of the SFD peaks, which were obtained from the first derivative of the partial hysteresis loop (dM/dH). The SFD of the top layer decreases with increasing top FePt layer thickness [Fig. 5(b)], suggesting an increased exchange coupling. Before discussing the results of the experimental comparison, we first describe a comparison of the model predictions of magnetization structures with experimental data

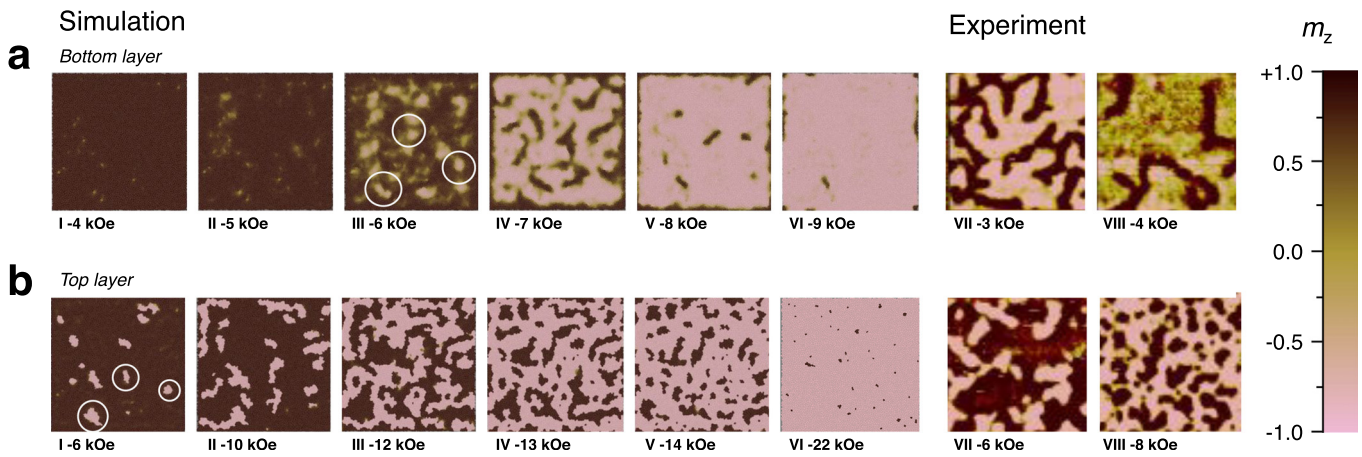

FIG. 6. Simulated and MFM magnetization conurations of the bottom (a) and top (b) layers in the trilayer structure with top FePt thickness of 20 nm and cross sectional area of $1.6 \times 1.6\ \mu m^2$ at different points of the hysteresis curve.

obtained using MFM. The aim is to ensure that the model predictions are consistent with experimental data at the microscopic as well as macroscopic level.

In order to compare the magnetic states of the hard and soft layers during switching, we present simulated and experimental MFM images of the reversal behavior of the individual layers with a top $L1_0$-FePt layer thickness of 20 nm in Fig. 6. Peng *et al.*[25] give a model formalism which allows interpretation of the magnetization structures in terms of the material parameters, especially the exchange. Reference 25 gives a study of cluster sizes in the ac erased state which, while not directly applicable to hysteresis properties, nonetheless provides a useful basis for discussion of the magnetization structures presented here. In particular, Peng *et al.* noted a tendency to the formation of stripe domains as seen here, with a domain width increasing with increasing exchange field. The cluster size was found to decrease with increasing values of the exchange decoupled fraction: an observation interpreted as arising from effective pinning sites at the decoupled grain boundaries, which imposed a limit on the domain expansion.

In Fig. 6, we show the magnetization structure for the bottom (a) and top (b) layers from the model calculations (left panels) and experiment (right panels). The MFM images in the experiment were taken after subjecting the fabricated PSV to an initial saturation field of kOe and a subsequent reversed field in the range of 0 to −8 kOe. At applied fields of −3 kOe and −4 kOe, reversal of the soft bottom FePt occurred, while the top hard FePt remained saturated [Fig. 4(h)]. Thus, Figs. 6(a-VII) and 6(a-VIII) capture the remanent magnetic configurations of the soft bottom FePt around its coercive field. At an applied field of −6 kOe, complete reversal of the soft bottom FePt took place [Fig. 4(h)] and the MFM probed only the magnetic configurations of the hard top $L1_0$-FePt. Hence, Figs. 6(b-VII) and 6(b-VIII) depict the remanent magnetic configuration of the hard top $L1_0$-FePt around its coercive field. Reversal proceeds via the formation and propagation of the reversed domains in both layers. It is to note that the simulated and MFM reversal configurations are compared at different fields due to the difference in coercivity of the $L1_0$-FePt layers between the simulated and fabricated PSV. Both the simulated and experimental results show good agreement in terms of the reversal mechanism, domain size, and shape. Larger domain sizes are observed for the bottom soft layer in both the simulation and experiment. According to Ref. 25, the different domain sizes relate to the magnitude of the intragranular exchange coupling and also the "pinning" effect of the presence of exchange decoupled grains. For agreement with experiment, the model calculations require a decoupled

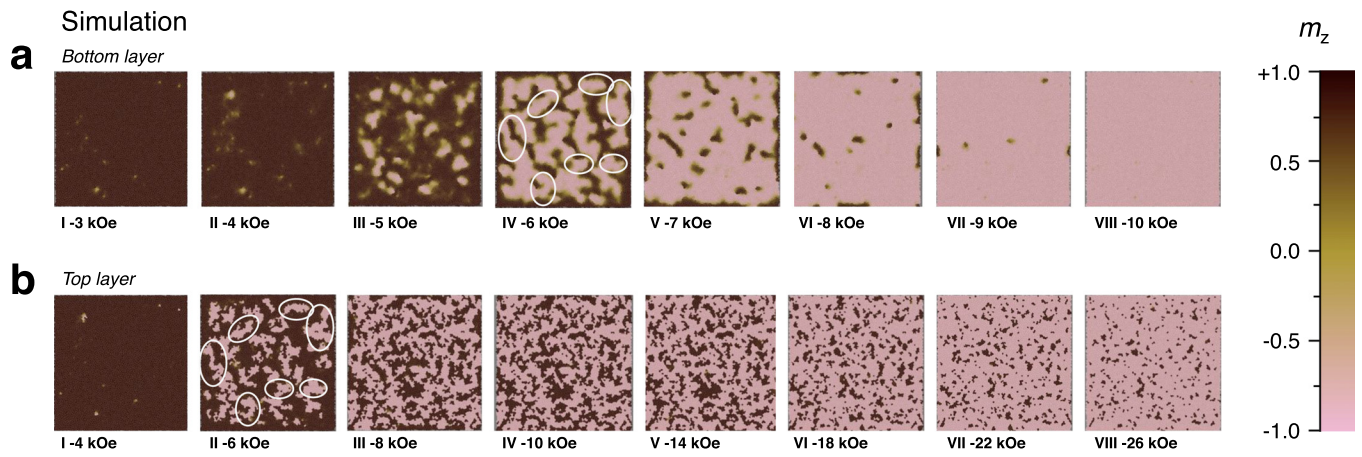

FIG. 7. Simulated magnetization conurations of the bottom (a) and top (b) layers in the trilayer structure with top FePt thickness of 5 nm and cross sectional area of $1.6 \times 1.6\ \mu m^2$ at different points of the hysteresis curve.

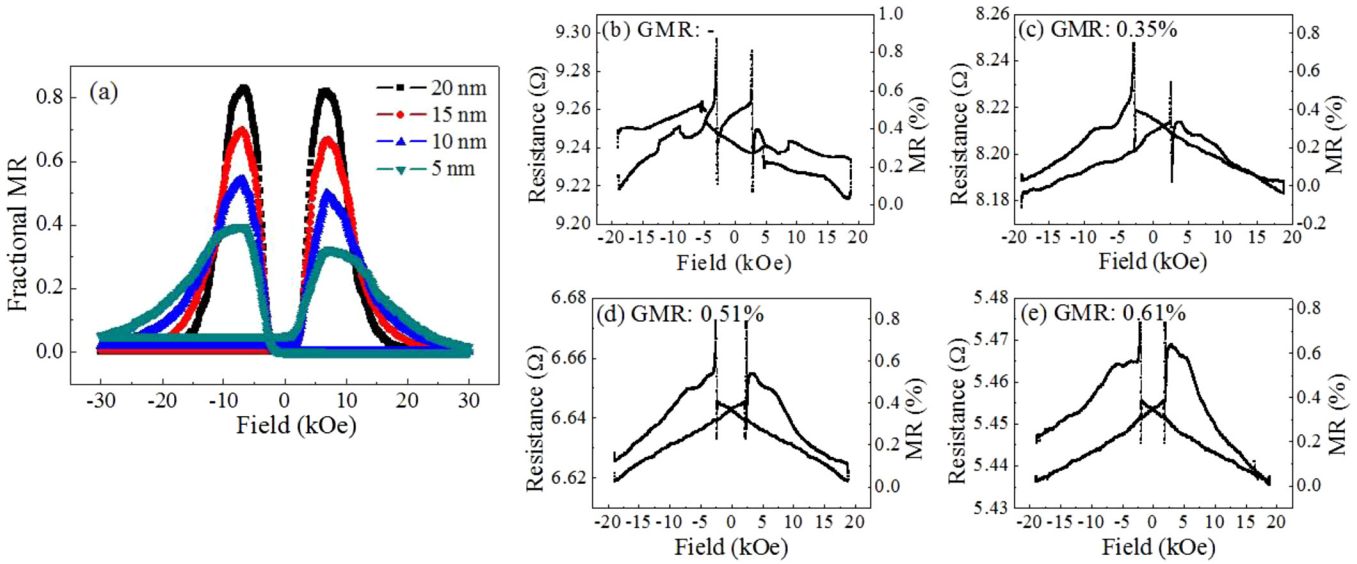

FIG. 8. (a) Magnetoresistance loops of the simulated trilayer with varying top FePt thickness. Current-in-plane magnetoresistance curves measured at room temperature for MgO/$L1_0$-FePt/TiN/$L1_0$-FePt PSVs with top $L1_0$-FePt thickness of (b) 5, (c) 10, (d) 15, and (e) 20 nm.[14]

fraction, within the bottom layer, of 0.01: essentially the grains are uniformly exchange coupled. This gives rise to domain propagation over long distances, resulting not only in larger domains but also in a smaller switching field distribution, consistent with Figs. 4(d) and 4(h).

This reversal behavior was compared with the calculated MFM images for a top hard layer thickness of 5 nm, which are shown in Fig. 7. The bottom and top FePt layers follow the same reversal mechanism as that with the 20 nm thick top FePt layer. The bottom layers of the simulated trilayers have the same input parameters but their calculated MFM images are not identical for the same reversal field (for instance, see Figs. 6(a-II) and 7(a-III) at field of 5 kOe). This is due to the slight deviation in the coercivity of the bottom layers [Fig. 5(a)], which is the result of the random distribution of the grain sizes and exchange coupling between grains during initialization with disorder introduced in the model. Nevertheless, the domain reversal process, size, and shape are similar in the soft bottom layers of both PSVs. On the other hand, the size of the reversed domains in the top thinner FePt appears smaller. This is attributed to the greater extent of independent reversal present within the thinner top FePt layer where the grains are more decoupled due to its granular morphology (Fig. 3). According to Peng *et al.*,[25] the domain size decreases with f_{intra}, which increases with decreasing grain size, reflecting the grain decoupling. It is interesting to note from Table I that the H_{int} is inversely proportional to the top FePt layer thickness. This is the expected behavior assuming a constant exchange coupling between the two layers and suggests that the nature of the interface is independent of the thickness of the top FePt layer, as seems reasonable.

B. Measurement and calculation of the magnetoresistance

Given an understanding of the influence of the hard layer thickness on the magnetic properties of the film, we now address the MR of the PSV. The perpendicular MR of the simulated PSVs is determined based on the difference in the magnetization angle between all the epitaxial grains, using the simple model[34]

$$\rho = \sum_{1}^{n} \frac{1 - \cos\phi}{2}, \tag{10}$$

where $\phi = \theta_{\text{bottom}} - \theta_{\text{top}}$ is the difference in the magnetization angle between each epitaxial grain on the adjacent FePt layers. The calculation assumes an excellent spin accumulation at the FePt/TiN interface, perfect FePt and TiN band structure compatibility, as well as a defect free crystal with a long spin diffusion length which does not contribute to spin independent flipping. A value of 1 for the fractional MR signifies that all the grains in the bottom FePt are oppositely magnetized with respect to the epitaxial grains in the top FePt.

Figure 8(a) shows the simulated fractional MR. CIP measurements indicate the existence of GMR for the thicker top layer samples, as shown in Figs. 8(b)–8(e). The fractional MR of the simulated trilayer is also observed to decrease with a thinner top FePt thickness [Fig. 8(a)]. This is in agreement with the measured MR trend [Figs. 8(b)–8(e)], where the decrease in GMR with the thinner top $L1_0$-FePt is understood in the experiment to be due to the lack of a continuous pathway for the spin dependent scattered electrons to be detected via the CIP measurement.[14] However, the effect of the continuity of electron percolation path is not taken into account in the MR calculation for the simulation, where the calculation of MR is carried out based on the angle made between the two adjacent top and bottom FePt grains. As such, the same MR trend observed from the simulation results is an indication of another possible contribution. As discussed in Sec. IV A, stronger interlayer exchange coupling and dipolar stray field coupling exist for the PSV with thinner top FePt layer. This suggests that in the PSV with a

TABLE II. A summary of the properties of the simulated trilayers with varying TiN spacer thickness of 3–7 nm.

TiN thickness (nm)	f_{inter}	Top K_u ($\times 10^7$ erg/cc)	Top f_{intra}
3	0.2	1.26	0.01
4	0.4	1.29	0.05
5	0.8	1.31	0.10
6	0.8	1.33	0.15
7	0.8	1.34	0.20

thinner top FePt layer, a greater proportion of domains in the bottom and top FePt layers possess parallel magnetization through stronger coupling, thus bringing about a smaller simulated fractional MR. Furthermore, the fact that the simulated MR calculations ignore the effects of continuity of the electron percolation pathway also leads to the discrepancy with the measured CIP MR. In particular, for the PSV with 5 nm top FePt, there exists a non-evident CIP GMR [Fig. 8(b)] compared to the significantly larger fractional MR in the corresponding simulated trilayer [Fig. 8(a)]. The simulation also does not consider magnon magnetoresistance, indicated by the sharp spike and dip in MR at the coercive field of the soft bottom $L1_0$-FePt.[14]

C. Variation of the TiN interlayer thickness

We now proceed to investigate the effects of spacer thickness on the hysteretic and magnetoresistive properties of the PSVs. In general, it is desirable that the two magnetic layers are decoupled so that the soft layer can be switched independently of the hard layer. By increasing the spacing thickness, one would expect the interlayer interactions to become weaker. However, the consequences for spin transport are non-trivial due to the non-insulating properties of the spacer.

In these simulated trilayers, the K_u of the bottom $L1_0$-FePt is constant at 8.48×10^6 erg/cc. Both the $L1_0$-FePt layers possess H_{intra} of 35 kOe, while a H_{int} of 1.2 kOe acts between the $L1_0$-FePt layers. A small dispersion fraction of 0.1 is introduced for the d_{inter} and d_{intra} of both the $L1_0$-FePt layers. The f_{intra} for the bottom $L1_0$-FePt is fixed at 0.01. The simulation results reveal that the f_{inter}, top FePt K_u, and top FePt f_{intra} are affected by the spacer thickness (Table II).

The change in TiN spacer thickness affects the extent of exchange coupled grains between the FePt layers, which is in turn influenced by the presence of pinholes. Pinhole defects can be thought of as localized regions where the roughness is greater than the thickness of the spacer, hence resulting in physical gaps which promote direct interactions between the FM layers. Surface roughness measurements were carried out on MgO/$L1_0$-FePt/TiN samples with TiN thickness of 3–7 nm. As seen in Table III, the root mean square roughness (R_{rms}) of the TiN spacer is negligibly small in the sub-nanometre scale and remained almost constant with different TiN thicknesses. Thus, orange peel coupling due to correlated roughness of the trilayer probably did not contribute significantly to the overall coupling. However, the maximum roughness (R_{max}) values generally increases with decreasing spacer thickness. In particular, for the TiN spacer thickness of 3 and 4 nm, the R_{max} is larger than the spacer thickness, thus suggesting the increasing presence of pinhole defects in thinner TiN spacer. The greater prevalence of pinhole defects in a thinner TiN spacer thereby creates a stronger direct exchange coupling. The magnitude of the H_{int} is a constant as the strength of the interlayer coupling acting across the layers would not change regardless of the spacer thickness. However, the influence of the interlayer coupling

TABLE III. Root-mean-square roughness (R_{rms}) and maximum roughness (R_{max}) values of MgO/$L1_0$-FePt/TiN surface with varying TiN layer thickness.[15]

TiN thickness (nm)	R_{rms} (nm)	R_{max} (nm)
3	0.27	6.44
4	0.28	5.58
5	0.30	4.46
6	0.26	3.75
7	0.29	4.82

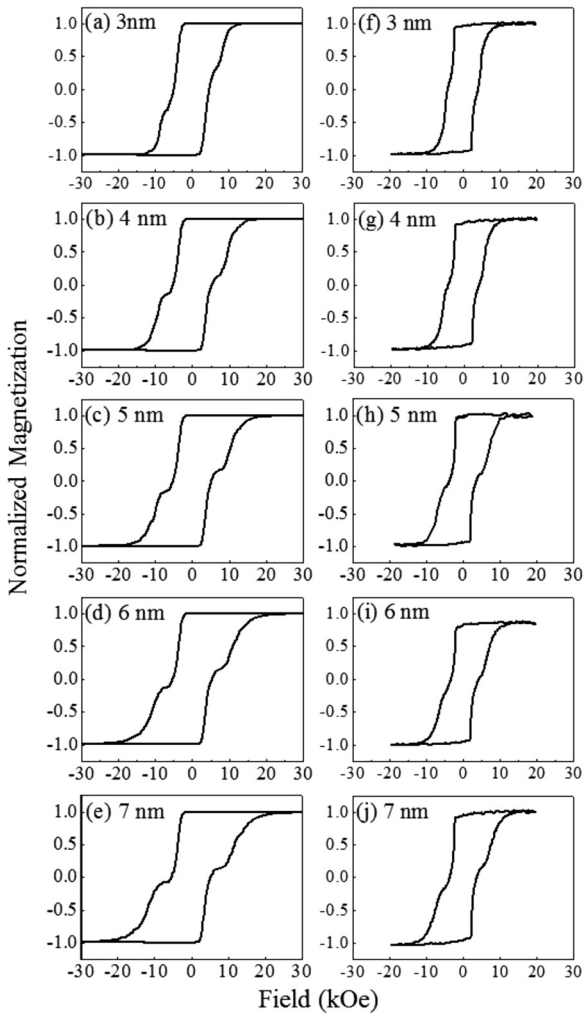

FIG. 9. Out-of-plane hysteresis loops with TiN spacer thickness of (a) 3, (b) 4, (c) 5, (d) 6, and (e) 7 nm for the simulated trilayer. Out-of-plane hysteresis loop measured at room temperature with TiN spacer thickness of (f) 3, (g) 4, (h) 5, (i) 6, and (j) 7 nm for the fabricated MgO/$L1_0$-FePt/TiN/$L1_0$-FePt PSVs with top layer thickness of 20 nm.[15]

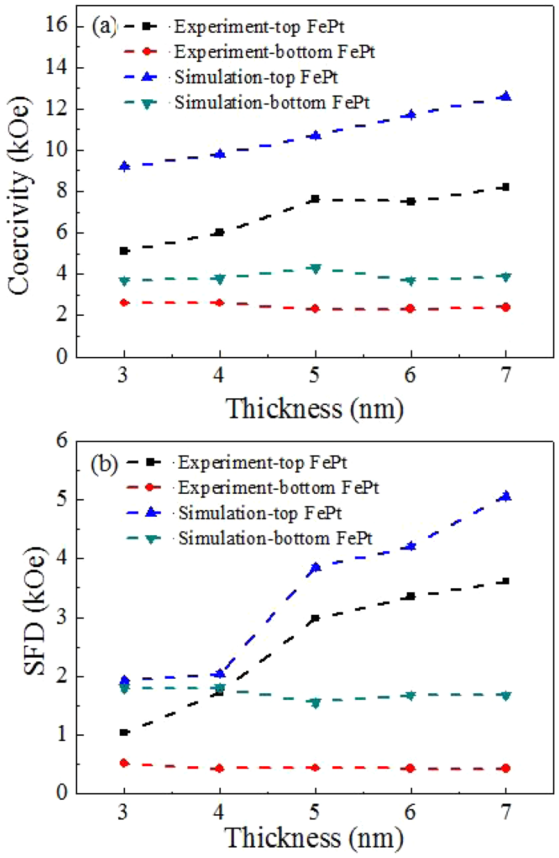

FIG. 10. (a) Coercivity and (b) SFD of the top and bottom FePt layers from simulation and experiment as a function of TiN spacer thickness. Dashed lines serve as a guide for the eyes.

increases with decreasing spacer thickness due to the increase in density of pinholes. The higher pinhole density is reflected in the greater fraction of exchange coupled grains formed between the FePt grains with reduced TiN spacer thickness.

In the simulated trilayers with varying TiN spacer thickness, the hysteresis loops [Figs. 9(a)–9(e)] show good agreement with experimental hysteresis loops [Figs. 9(f)–9(j)]. With increasing spacer thickness, the PSVs become increasingly well-decoupled. At the same time, the coercivity and the switching field distribution of the top FePt layer also increase [Fig. 10]. A change in the spacer thickness also affects the ordering of the top $L1_0$-FePt. It has been reported that the degree of TiN (200) orientation increases with increasing TiN film thickness, possibly due to the presence of fewer defects.[35] This in turn induces a larger degree of *c*-axis (001) orientation and thus higher H_c and K_u of the FePt layer grown on the TiN. Furthermore, the top FePt could also assume a less interrupted and more continuous growth from the bottom FePt with a thinner TiN. As such, a smoother and more continuous top $L1_0$-FePt layer with a smaller extent of intralayer exchange decoupled grains is observed.

With increasing TiN thickness, the change in simulated fractional MR is marked with an initial sharp increase followed by a more gradual one (Fig. 11). The increasingly well decoupled trilayer with increasing TiN thickness allows the bottom softer FePt layers to reverse more independently

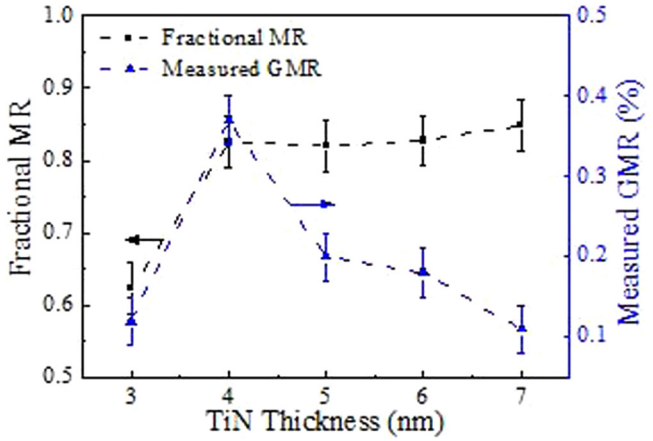

FIG. 11. Fractional MR of the simulated trilayers (■) and measured GMR (Ref. 15) (▲) of the MgO/$L1_0$-FePt/TiN/$L1_0$-FePt PSVs with respect to different TiN spacer thicknesses. Dashed lines serve as a guide for the eyes.

due to the weaker influence of the top harder FePt layer. This gives rise to a greater proportion of interlayer adjacent grains with opposite spins when the trilayer assumes an antiparallel conuration, bringing about an increase in MR. However, the fractional MR trend deviates from the GMR trend measured via CIP at room temperature, which shows an initial increase followed by a subsequent decline in GMR. Taking into consideration the relatively large TiN electron mean free path (39–41 nm) with respect to its thickness (3–7 nm), we believe that the spin independent scattering of conduction electrons within the spacer is unlikely to have contributed to the reduction of GMR with the increase in TiN thickness. Instead, it is likely that the experimentally measured GMR diminishes with increasing spacer thickness due to current shunting effects, where electrons preferentially flow through the spacer instead of undergoing scattering at the $L1_0$-FePt/TiN interfaces. The deviation between the calculated and simulated MR is due to the fact that the MR calculation does not account for the electron transport component, considering only the magneto component in the spin-electronic system.

V. CONCLUSION

A micromagnetic trilayer model which utilizes the LLB equation of motion is used to study the crystallographic texture, magnetic properties, reversal behavior, interlayer coupling effects, and spin transport properties of the $L1_0$-FePt/TiN/$L1_0$-FePt PSVs, with varying top $L1_0$-FePt and TiN spacer thickness. The intralayer coupling properties of the FM layers, mediated by the interactions within the granular layer, affect the performance of the PSV. A more granular FM layer, with a single domain per grain, displays a higher coercivity but introduces a larger switching field distribution and longer magnetic tail on saturation. These are the direct effects of the increasing susceptibility of a more granular FM layer, with smaller and greater number of grains, to demagnetization under the influence of dipolar stray fields. As a result, the PSVs with increasingly granular FM layer are associated with lower MR.

We have also found that optimizing the operation of a PSV requires a delicate balance of separating the layers sufficiently so that each may be controlled separately, while still allowing sufficient current flow to contribute to magnetoresistance. Even in the case of exchange decoupling of the two layers by using TiN, the dipolar field from each layer is sufficient to couple them and reduce the effective magnetoresistance.

In summary, we have demonstrated through parallel experimental work and micromagnetic simulations that the interlayer and intralayer interactions of the FM layers in the PSV, in association with the spacer thickness and FM layer thickness, affect the performance of the PSV. A good control of the physical structure of the PSV is essential for catering to specific requirements of individual spintronics applications.

ACKNOWLEDGMENTS

This work is partially supported by Ministry of Education, Singapore, Grant No. MOE2012-T2-2-031 and the Singapore National Research Foundation under CPR Award No. NRF-CRP10-2012-02. Financial support from the EU Seventh Framework Programme under Grant Agreement No. 281043 femtospin is also gratefully acknowledged.

[1]C. Chappert, A. Fert, and F. N. V. Dau, Nature Mater. **6**, 813 (2007).
[2]A. D. Kent, Nature Mater. **6**, 399 (2007).
[3]M. Tsoi, Nat. Phys. **4**, 17 (2008).
[4]S. M. Thompson, J. Phys. D: Appl. Phys. **41**, 093001 (2008).
[5]J. G. Zhu, Proc. IEEE **96**, 1786 (2008).
[6]S. Mangin, D. Ravelosona, J. A. Katine, M. J. Carey, B. D. Terris, and E. E. Fullerton, Nature Mater. **5**, 210 (2006).
[7]J. Z. Sun, IBM J. Res. Dev. **50**, 81 (2006).
[8]P. de Person, P. Warin, M. Jamet, C. Beige, and Y. Samson, Phys. Rev. B **76**, 184402 (2007).
[9]R. Sbiaa, H. Meng, and S. N. Piramanayagam, Phys. Status Solidi RRL **5**, 413 (2011).
[10]P. Ho, G. C. Han, R. F. L. Evans, R. W. Chantrell, G. M. Chow, and J. S. Chen, Appl. Phys. Lett. **98**, 132501 (2011).
[11]A. P. Mihai, J. P. Attane, L. Vila, C. Beigne, J. C. Pillet, and A. Marty, Appl. Phys. Lett. **94**, 122509 (2009).
[12]M. Yoshikawa, E. Kitagawa, T. Nagase, T. Daibou, M. Nagamine, K. Nishiyama, T. Kishi, and H. Yoda, IEEE Trans. Magn. **44**, 2573 (2008).
[13]T. Seki, S. Mitani, K. Yakushiji, and K. Takanashi, Appl. Phys. Lett. **88**, 172504 (2006).
[14]P. Ho, G. C. Han, K. H. He, G. M. Chow, and J. S. Chen, Appl. Phys. Lett. **99**, 252503 (2011).
[15]P. Ho, G. C. Han, K. H. He, G. M. Chow, and J. S. Chen, J. Appl. Phys. **111**, 083909 (2012).
[16]K. O'Grady, L. E. Fernandez-Outon, and G. Vallejo-Fernandez, J. Magn. Magn. Mater. **322**, 883 (2010).
[17]P. Ho, G. C. Han, R. F. L. Evans, R. W. Chantrell, G. M. Chow, and J. S. Chen, IEEE Trans. Magn. **47**, 2646 (2011).
[18]P. Ho, G. C. Han, R. F. L. Evans, R. W. Chantrell, G. M. Chow, and J. S. Chen, Appl. Phys. Lett. **99**, 162503 (2011).
[19]D. A. Garanin, Phys. Rev. B **55**, 3050 (1997).
[20]N. Kazantseva, D. Hinzke, U. Nowak, R. W. Chantrell, U. Atxitia, and O. Chubykalo-Fesenko, Phys. Rev. B **77**, 184428 (2008).
[21]R. F. L. Evans, D. Hinzke, U. Atxitia, U. Nowak, R. W. Chantrell, and O. Chubykalo-Fesenko, Phys. Rev. B **85**, 014433 (2012).
[22]E. Yang and D. E. Laughlin, J. Appl. Phys. **104**, 023904 (2008).
[23]F. Burrows, C. Parker, R. F. L. Evans, Y. Hancock, O. Hovorka, and R. W. Chantrell, J. Phys. D: Appl. Phys. **43**, 474010 (2010).
[24]M. L. Plumer, J. van Lierop, B. W. Southern, and J. P. Whitehead, J. Phys.: Condens. Matter **22**, 296007 (2010).
[25]Y. Peng, X. W. Wu, J. Pressesky, G. P. Ju, W. Scholz, and R. W. Chantrell, J. Appl. Phys. **109**, 123907 (2011).
[26]V. Sokalski, D. E. Laughlin, and J.-G. Zhu, Appl. Phys. Lett. **95**, 102507 (2009).
[27]R. F. L. Evans, Q. Coopman, S. Devos, W. J. Fan, O. Hovorka, and R. W. Chantrell, J. Phys. D: Appl. Phys. **47**, 502001 (2014).
[28]V. Baltz, A. Marty, B. Rodmacq, and B. Dieny, Phys. Rev. B **75**, 014406 (2007).
[29]L. Thomas, M. G. Samant, and S. S. P. Parkin, Phys. Rev. Lett. **84**, 1816 (2000).
[30]S. Wiebel, J. P. Jamet, N. Vernier, A. Mougin, J. Ferre, V. Baltz, B. Rodmacq, and B. Dieny, Appl. Phys. Lett. **86**, 142502 (2005).
[31]W. S. Lew, S. P. Li, L. Lopez-Diaz, D. C. Hatton, and J. A. C. Bland, Phys. Rev. Lett. **90**, 217201 (2003).
[32]L. Thomas, J. Luning, A. Scholl, F. Nolting, S. Anders, J. Stohr, and S. S. P. Parkin, Phys. Rev. Lett. **84**, 3462 (2000).
[33]M. P. Sharrock, J. Appl. Phys. **76**, 6413 (1994).
[34]B. A. Gurney, M. Carey, C. Tsang, M. Williams, S. S. P. Parkin, R. E. Fontana, Jr., E. Grochowski, M. Pinarbasi, T. Lin, and D. Mauri, *Ultrathin Magnetic Structures IV*, edited by B. Heinrich and J. A. C. Bland (Springer, Berlin, 2005), Chap. 6, p. 2.
[35]Y. Tsuji, S. Noda, and Y. Yamaguchi, J. Vac. Sci. Technol. B **25**, 1892 (2007).